Low-cost chitosan-calcite adsorbent development for potential phosphate removal and recovery from wastewater effluent

Low-cost chitosan-calcite adsorbent development for potential phosphate removal and recovery from wastewater effluent

Sabolc Pap[a,b,*], Caroline Kirk[c], Barbara Bremner[a], Maja Turk Sekulic[b], Lisa Shearer[a], Stuart W. Gibb[a], Mark A. Taggart[a]

[a] *Environmental Research Institute, North Highland College, University of the Highlands and Islands, Thurso, Caithness, Scotland, KW14 7JD, UK*

[b] *University of Novi Sad, Faculty of Technical Sciences, Department of Environmental Engineering and Occupational Safety and Health, Trg Dositeja Obradovića 6, 21 000 Novi Sad, Serbia*

[c] *School of Chemistry, University of Edinburgh, David Brewster Rd, Edinburgh, EH9 3FJ, UK*

[*] Corresponding author at:
Environmental Research Institute, North Highland College, University of the Highlands and Islands, Scotland, KW14 7JD, UK
E-mail: szabolcs.pap@uhi.ac.uk; sabolcpap@uns.ac.rs
Telephone: 01847 889676; Fax: 01847 890014;
ORCID: 0000-0001-7395-1913;
Notes: The authors declare no competing financial interests

Abstract

Phosphorous (P) recovery from wastewater will become increasingly vital in the future as terrestrial rock phosphate deposits are expended. Effective management of P as a critical resource will require new techniques to recover P from wastewater, ideally in a form that can be used in agriculture as fertiliser. In this study, batch and fixed-bed column conditions were tested using a novel KOH deacetylated calcite-chitosan based adsorbent (CCM) for P removal from aqueous solutions and wastewater effluents. The unique characteristics of this adsorbent as a phosphate adsorbent were the result of rich surface functionality (amine and sulphur functional groups of the chitosan and proteins) and the $CaCO_3$ content (providing donor ligands; and additionally beneficial if the material were used as fertiliser, buffering soil acidification caused by nitrogen application). The maximum P adsorption capacity was determined to be 21.36 mgP/g (at 22 °C) and the endodermic process reached equilibrium after 120 min. The experimental data was best described using a Langmuir isotherm and a pseudo-second order kinetic model. The diffusion kinetic analysis highlighted the importance of both film and intraparticle mass-transport. Material characterisation suggested that the adsorption process involved interactions between P and functional groups (mostly $-NH_3^+$) due to electrostatic interaction on the chitosan chain or involved ligand exchange with CO_3^{2-}. Analysis of materials using X-Ray Powder Diffraction (XRPD) and Thermogravimetric Analysis (TGA) indicated a microprecipitation-type mechanism may occur through the formation of hydroxylapatite ($Ca_5(PO_4)_3(OH)$). Desorption studies demonstrated that the P-laden CCM (derived from crab carapace) had the potential to be reused in soil amendment as a slow-release P fertiliser. The effects of different operating parameters were explored in a fixed-bed column, and the experimental data fitted well to the Clark model (R^2 = 0.99).

The CCM also showed excellent P adsorption potential from secondary and final wastewater effluent in dynamic conditions, even at low P concentrations. Finally, a scale-up approach with cost analysis was used to evaluate the price and parameters needed for a potential large-scale P recovery system using this adsorbent.

Keywords: Wastewater treatment; critical resource management; column study; phosphate desorption; secondary phosphorus fertiliser

1. Introduction

Wastewater effluent from rural and urban activities is often high in phosphorous (P) - a potential pollutant of freshwater which may contribute to eutrophication (Haddad et al., 2018). The European Union seeks to limit total P concentrations in wastewater effluent to ~1-2 mg/L (Directives 91/271/EEC and 98/15/EEC on Urban Waste Water Treatment), for less sensitive receiving waters (Wang et al., 2018). However, P concentrations often need to be lower (below 15 µg/L) to avoid ecological imbalance in algal, macrophyte and macroinvertebrate assemblages (Richardson et al., 2007). In parallel, P is also a vital soil nutrient, critical in modern agriculture and food production, but is a finite resource - largely obtained from rapidly dwindling terrestrial rock phosphate reserves. Schröder et al. (2011) have estimated that by 2035, global P demand will exceed supply, and as such (and in line with principles of the "*circular economy*") there is an urgent need to use and re-use P more efficiently, and where possible, to recover P from waste streams, including wastewater.

Numerous P removal methods have been used in wastewater treatment, including biological treatment (Yang et al., 2018), chemical precipitation and crystallisation (Huang et al., 2017), membrane technologies (Furuya et al., 2017), constructed wetlands (Du et al., 2017), ion exchange (Bui et al., 2018) and adsorption (Yu et al., 2017). When

compared to biological treatment, chemical precipitation is potentially more effective; however, the sludge produced following chemical precipitation may cause significant secondary waste/pollution. Biological treatment, due to the dependence on P accumulating biota (i.e., algae, microbes, plants) is challenging to optimise and achieve consistently which may result in a failure to satisfy strict discharge requirements without further treatment (Ajmal et al., 2018). Moreover, biological and chemical treatments may not be suitable for P removal at low concentrations (Alshameri et al., 2014) and more advanced solutions (e.g., ion exchange and membrane processes) can be prohibitive due to their high costs and energy consumption.

Adsorption processes can be efficient, cost effective and sustainable for P removal, even at low P concentrations (Mitrogiannis et al., 2018). However, adsorption efficiency and interaction mechanisms are dependent on the nature of the adsorbent used, and on the process conditions (e.g., pH, concentration) (Paunovic et al., 2019). Many synthesised adsorbents have been investigated recently, including those based on crosslinked chitosan-Fe(III) complex sorbents (Zhang et al., 2018); calcium hydroxide treated clinoptilolite (Mitrogiannis et al., 2017); pyrolysed crab shell (Dai et al., 2017); chitosan beads (Liu and Zhang, 2015); and, scallop shells (Yeom and Jung, 2009). Raw materials with a high content of multivalent metal elements (e.g., calcium (Ca), magnesium (Mg) and aluminium (Al)), and, a rich surface chemistry (e.g., amine groups, $–NH_2$ may provide better solutions when compared with traditional biochars or activated carbons made from lignocellulosic biomass (Dai et al., 2017). Recovery of P through adsorption onto natural waste materials (such as crab carapace) may provide an alternative low-cost solution, and one that may involve the generation of a P-rich product low in other

adsorbed contaminants. In creating such a material, potential would then exist to use this as a secondary P fertiliser for soil amendment.

To address the combined challenges of P removal at relatively low concentrations (0.1–5 mg/L), the prevention of eutrophication (in receiving waters) and produce a P-enriched material potentially suitable as fertiliser, this study evaluates P adsorption from synthetic solutions and from wastewater effluents using a calcite-chitosan based adsorbent (CCM). The novelty of this research is reflected through the selection of the source material, crab carapace, and the low-cost synthesis methodology used. Crab carapace has previously been tested as a biosorbent for heavy metal and radionuclide removal (e.g., Lu et al., 2007; Rae et al., 2019, 2009), however, its potential for phosphate removal has not yet been reported. Furthermore, preparation costs (due to the low temperature used) were comparatively low, again an important commercial benefit. As well as adsorption, we also studied desorption of P using two acidic eluents and water, to consider secondary use of this material as a potential P-rich fertiliser. A range of instrumental techniques such as Scanning Electron Microscopy with Energy Dispersive X-ray Spectroscopy (SEM/EDX), Brunauer-Emmett-Teller technique (BET), X-ray Powder Diffraction (XRPD), Fourier Transform Infrared Spectroscopy (FTIR) and Thermal Gravimetric Analysis (TGA) were used to explore the observed adsorption mechanisms. Dynamic adsorption behaviour was explored in a column study - varying bed height, initial P concentration and flow rate; while potential costs and scale-up are considered and key parameters calculated for use in a pilot-scale column treatment system.

2. Material and Methods

2.1. Adsorbent synthesis

Previous reports have demonstrated the effectiveness of chitosan in the uptake of P as well as other oxyanions and metals (e.g., arsenate, arsenite, and strontium) (Jiang et al., 2013; Kumar and Jiang, 2016). The binding capacity of chitosan to P is largely due to amine groups present on the chitosan chain, which can serve as coordination sites for many oxyanions.

The parent material for the chitosan-calcite adsorbent used here was brown crab (*Cancer pagurus*) carapace collected as seafood waste from Scrabster (Scotland). The chitosan-calcite adsorbent was created from the raw carapace through thermochemical modification with deacetylation of the chitin chain in the presence of potassium hydroxide (KOH) (Pap et al., 2020). Deacetylation of chitin to chitosan is represented by Fig. S1. Briefly, raw carapace material was washed (with tap water), dried, milled and sieved to <250 µm (for batch experiments) and 0.5-1 mm (for column studies). 50 g of each sieved material was then mixed with KOH solution (impregnation ratio: 0.1 g KOH/g raw material by weight). The resulting impregnated material was then heated at 105°C for 150 min. After cooling, the resultant material was rinsed with Type I water (Milli-Q® Direct 8 system) to eliminate any by-products or residues, dried at 60 °C for a further 2 h, and then stored in glass bottles. The final adsorbent is referred to here as CCM (Crab Carapace Modified). A schematic diagram presenting the process used to prepare the CCM is shown in Fig. S1.

2.2. Materials, analytical methods, wastewater effluent and adsorption mechanism analysis

All chemicals used were of analytical grade. Phosphate (1000 mg P/L) stock solutions were prepared using potassium dihydrogen phosphate and Milli-Q® water. Residual P

129 concentrations were measured using a SEAL AQ2 Discrete Analyser (Seal Analytical,
130 UK) utilising the antimony-molybdate reaction with ascorbic acid as the reductant. The
131 resultant blue colour was measured at a wavelength of 880 nm (APHA, 2005). Inductively
132 coupled plasma optical emission spectroscopy (ICP-OES; Varian 720-ES) was used to
133 determine dissolved metal concentrations in wastewater effluent samples. The
134 instruments were calibrated within their linear ranges (correlation coefficients >0.98);
135 blanks and external standards were used to ensure QA/QC.
136 Secondary wastewater effluent was collected from Wick Wastewater Treatment Plant
137 (WWTP), Caithness, Scotland, a facility operated by Scottish Water. The WWTP has a
138 design capacity of 13,500 PE (population equivalents), with an advanced biological
139 treatment (Cyclic Activated Sludge System, CASS™) process. Final wastewater effluent
140 was obtained from Bo'ness WWTP Development Centre (Scottish Water), Scotland, to
141 test potential P adsorption at low effluent concentrations. The concentration of P in this
142 effluent was 0.837 mg/L. After sampling, effluent samples were immediately transported
143 to the laboratory and adsorption experiments conducted within 24 hours. The
144 characteristics of the secondary wastewater effluent sample are presented in Table S1.
145 CCM (before and after P adsorption) was characterised to aid understanding of the
146 adsorption mechanisms involved. Material after P adsorption was collected during the
147 isotherm studies, wherein an initial P concentration of 50 mg/L and initial pH 7 (no further
148 pH adjustment) was used, followed by rinsing with Milli-Q® water and drying at 70 °C.
149 The micro-structures of the CCM were characterised using SEM: Topcon SM-300,
150 equipped with energy-dispersive X-ray analysis (EDX). BET specific surface area and
151 pore size distribution were determined based on N_2 adsorption-desorption using an
152 Autosorb iQ instrument (Quantachrome, USA). XRPD data were collected using a Bruker

D2 Phaser X-ray powder diffractometer in reflection geometry with Cu Kα radiation (1.5418 Å) over the two-theta range 6-60° for a total collection time of 10 minutes. Fourier-transform infrared (FTIR) spectra were recorded at room temperature using a Perkin Elmer Spectrum FTIR Spectrometer over the range 500-4500 cm^{-1}. Thermogravimetry was carried out using a computer-controlled thermogravimetric analyser (STA 449 C Jupiter – Netzsch) over the temperature range of room temperature to 1000 °C under air/nitrogen.

2.3. P adsorption experiments

2.3.1. P adsorption in a batch system

To assess the effect of pH on adsorption of P, 200 mg of CCM was added to 50 mL of P solution (20 mg/L P) in Erlenmeyer flasks. The pH of solutions was adjusted within the range of 2.0 – 12.0 with 0.1 M HCl or NaOH. Flasks were then placed on an orbital shaker (IKA KS 260) at 150 rpm for 120 min at room temperature (22 °C). After filtration using a 0.45 μm polytetrafluoroethylene (PTFE) syringe filter (Fisher Scientific, UK), the percentage of P removal, R (%), and the equilibrium adsorption capacity, q_e (mg P/g), were determined using:

$$R\ (\%) = \frac{C_0 - C_e}{C_0} \cdot 100 \quad (1)$$

$$q_e = \frac{(C_0 - C_e)}{m} \cdot V \quad (2)$$

Where C_0 is the initial P concentration, C_e is the residual concentration (mg P/L), V is the volume of solution (L) and m is the mass of the CCM (g) used.

Adsorption kinetics were investigated using 500 mg of CCM in 500 mL of P solution (20 mg P/L) at two different temperatures (22 and 42 °C). Solution pH was not adjusted, and

175 the Erlenmeyer flasks were shaken at 150 rpm. Over a 300 min contact period, at
176 predetermined time intervals (1, 5, 15, 30, 45, 60, 90, 120, 180, 240 and 300 min), samples
177 were taken.
178 Adsorption isotherms were created at three different temperatures (22, 32 and 42 °C)
179 using 100 mL solutions containing different initial P concentrations (in the range 1–50
180 mg P/L) with a CCM dose of 100 mg.
181 The effect of individual coexisting anions on P adsorption was studied in 50 mL solutions
182 containing 20 mg P/L and 20 mg/L of each of the following anions: NO_3^-, Cl^-, CO_3^{2-} and
183 SO_4^{2-} (total ion concentration of 100 mg/L).
184 P desorption experiments were conducted by first adding 100 mg of adsorbent into 50 mL
185 of 50 mg/L P solution, then shaking for 2 h. The resultant P-loaded CCM was then
186 separated from the suspension by centrifugation at 4000 rpm for 10 min. The P-laden
187 CCM was then desorbed using 3 different solutions separately, (a) 2% citric acid, (b)
188 0.5M HCl, and (c) Milli-Q® water – using a liquid: solid ratio of 500 mL/g (i.e., 0.1 g in
189 50 mL of eluent) at 22 °C. After 2 h contact time, eluent supernatants were removed and
190 measured for P concentration. At the same time, blank experiments were carried out to
191 quantify the 'background' P dissolved from the primary adsorbent. At a given time, *t*, the
192 desorption efficiency (d_E (%)) and the P released (q_d (mg P/g)) were calculated using the
193 following:

194 $$d_E = \frac{q_d}{q_a} \cdot 100 \quad (3)$$

195 $$q_d = \frac{C_{t,des}}{m} \cdot V \quad (4)$$

196 Where q_d (mg P/g) is the amount of P desorbed, q_a (mg P/g) is adsorption capacity, $C_{t,\,des}$
197 (mg/L) is the P concentration in the desorbed solution, V (L) is the volume of solution
198 used, and m (g) is the amount of pre-loaded CCM.

199 *2.3.2. P adsorption in a dynamic system*

200 Dynamic column studies were conducted at room temperature using glass columns (20
201 cm length, 2 cm internal diameter). Glass wool was placed at the bottom and top of the
202 column to prevent adsorbent washout. P working solutions were continuously fed in an
203 up-flow mode (See Fig S2 in Supplementary Materials) into the column by peristaltic
204 pump (Masterflex, Cole-Parmer Instrument Co., USA). The influent contained different
205 P concentrations (5, 10, and 20 mg P/L) and was passed through varying column bed-
206 heights (3, 6 and 10 cm) using three flow rates (3.5, 7.0, and 10.5 mL/min). Samples were
207 collected at regular time intervals (using an ISCO Foxy Junior fraction collector) in order
208 to obtain breakthrough curves. The breakthrough time (t_b) was taken when the outlet P
209 concentration attained 10% of the inlet concentration, while the exhaustion time (t_e) was
210 determined when the effluent P level reached 90% of the inlet concentration. The
211 maximum column capacity, q_{total} (mg) for a given set of conditions was calculated from
212 the area under the plot for the adsorbed P concentration, C_{ad} (mg P/L), versus time, as
213 given by:

214 $$q_{total} = \frac{QA}{1000} = \frac{Q}{1000}\int_{t=0}^{t=t_{total}} C_{ad}\,dt \qquad (5)$$

215 Where $C_{ad} = C_i - C_e$ (mg/L), t_{total} is the total flow time (min), Q is the flow rate (mL/min)
216 and A is the area under the breakthrough curve (cm^2).

217 The equilibrium uptake (q_{eq}), i.e., the amount of P adsorbed (mg) per unit dry weight of
218 adsorbent (mg P/g) in the column, was given by the equation:

$$q_{\mathrm{eq}} = \frac{q_{\mathrm{total}}}{W} \quad (6)$$

Where W is the total amount of adsorbent (g) in the column.

A further description of the column operating conditions is given in Supplementary Materials. Each adsorption experiment was carried out in triplicate, and the data were reported as means. Chi-square (χ^2) and root mean square error (*RMSE*) tests were used to analyse the errors within the data (see Supplementary Materials).

3. Results

3.1. Batch P adsorption onto CCM

The influence of initial P concentration on P adsorption onto the CCM was investigated within a concentration range from 1.0 to 50 mg P/L, at three different temperatures. As shown in Fig. 1a, P adsorption capacity gradually increased as the initial P concentration and temperature increased. Maximum adsorption capacities were 21.56, 23.88 and 24.85 mg P/g at 22, 32 and 42 °C, respectively. Values for $q_{0.1}$ showed the adsorption capacities that will be achieved at lower phosphate concentrations (Table 1). These capacities are observed at equilibrium concentrations lower than 0.1 mg P/L, which are realistic when thinking in the context of effluent polishing (Kumar et al., 2019). Further, P adsorption behaviour was explored using two isotherm models (Langmuir and Freundlich; see Supplementary Materials) and the curves at different operating temperatures are provided in Fig. 1a. The isotherm model parameters obtained using the nonlinear regression method, alongside the correlation coefficients (R^2) and the statistical errors (*RMSE* and χ^2) are listed in Table 1.

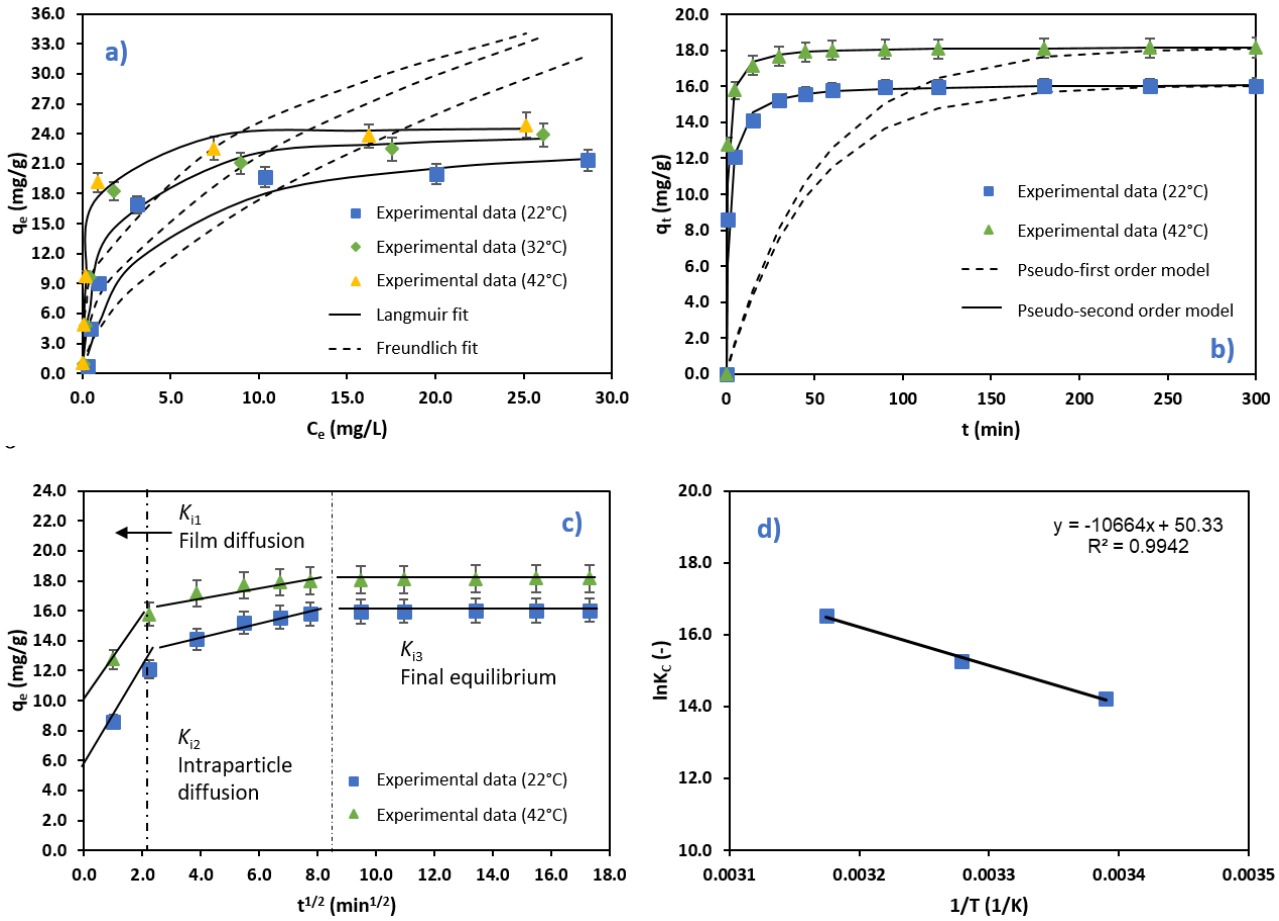

Fig. 1. Batch adsorption experimental results: (a) adsorption equilibrium data, (b) adsorption reaction kinetics, (c) Weber-Morris (WB) intraparticle diffusion model and (d) van't Hoff plot for P adsorption onto CCM (initial concentration: 1–50 mg P/L; no pH adjustment; contact time: 1-300 min; dose of adsorbent: 1 g/L; rotation speed: 150 rpm - Note: the data (n = 3) are represented as mean ± standard error).

Table 1

Parameters corresponding to P adsorption isotherms using CCM and three different temperatures.

Parameters		Temperature (°C)		
		22	32	42
$q_{max,exp}$ (mg /g)		21.36	23.88	24.85
Langmuir	q_{max} (mg P/g)	24.14	24.68	24.84

	$q_{0.1}$ (mg P/g)	0.88	1.79	5.48
	K_L (L/mg)	0.38	0.78	2.83
	R^2	0.94	0.99	0.99
	χ^2	0.45	0.06	0.01
	RMSE	0.13	0.03	0.01
Freundlich	K_F (mg/g)/(mg/L)^n	4.65	7.48	11.50
	1/*n*	0.57	0.46	0.34
	R^2	0.72	0.76	0.92
	χ^2	1.01	0.73	0.26
	RMSE	0.31	0.28	0.16

Adsorption kinetics consider the rate of adsorption and help define likely reaction/mass-transfer mechanisms (Turk Sekulic et al., 2019). As shown in Fig. 1b, rapid adsorption is observed in the first 5 minutes, then, adsorption slows down. The CCM-P system reached equilibrium after ~120 mins (Fig. 1b). In addition, higher temperatures (22→42°C) had a positive influence on P removal. These kinetic experimental results were fitted to pseudo-first order (PFO) and pseudo-second order (PSO) reaction models. Subsequently, to explore mass-transfer mechanisms from the bulk solution to the active sites within the inner pores, the Weber-Morris (WB) intraparticle diffusion model was also used (see Supplementary Materials). Plots of the reaction kinetic models and WB intraparticle diffusion model are shown in Fig. 1b and 1c (respectively), while the model parameters are listed in Table 2.

Table 2

Kinetic model parameters for P adsorption onto CCM at two different temperatures

Parameters	Temperature (°C)	
	22	42

$q_{e,exp}$ (mg P/g)		16.05	18.16
Pseudo-first order	$q_{t,cal}$ (mg P/g)	1.59	0.94
	k_1 (min^{-1})	0.02	0.02
	R^2	0.87	0.89
	χ^2	5.15	20.20
	RMSE	0.37	0.36
Pseudo-second order	$q_{t,cal}$ (mg P/g)	16.14	18.20
	k_2 (g/mg min)	0.04	0.08
	h (mg/g min)	9.90	25.17
	R^2	0.99	0.99
	χ^2	0.02	0.01
	RMSE	0.03	0.01
Weber–Morris intraparticle diffusion model	k_{i1} (mg/g $min^{1/2}$)	1.23	0.85
	C_1 (mg/g)	9.33	13.87
	R^2	0.99	0.99
	k_{i2} (mg/g $min^{1/2}$)	0.14	0.05
	C_2 (mg/g)	14.65	17.58
	R^2	0.95	0.94
	k_{i3} (mg/g $min^{1/2}$)	0.01	0.01
	C_3 (mg/g)	15.85	17.97
	R^2	0.99	0.97
Activation energy	E_a (kJ/mol)	26.19	

The activation energy for P adsorption onto CCM (E_a; kJ/mol) can be determined using the Arrhenius equation. This describes the minimum energy that the adsorbent - adsorbate system must have for the interaction to proceed. Based on adsorption kinetic experiments performed at two temperatures (Table 2):

$$K = Ae^{-E_a/RT} \quad (7)$$

$$lnk_{2(42°C)} - lnk_{2(22°C)} = \left(lnA - \frac{E_a}{RT_{42°C}}\right) - \left(lnA - \frac{E_a}{RT_{22°C}}\right)$$

$$\Leftrightarrow E_a = \frac{Rln\frac{k_{2(42°C)}}{k_{2(22°C)}}}{\frac{1}{T_{22°C}} - \frac{1}{T_{42°C}}} \quad (8)$$

Where $k_{2(42°C)}$ and $k_{2(22°C)}$ are the rate constants of the PSO model at 42°C and 22°C, respectively; A is the temperature independent Arrhenius factor, R is the universal gas constant (8.314 J/mol K); and T is the absolute temperature in K. The magnitude of the activation energy required gives an indication of the type of adsorption occurring, i.e., whether mainly physical or chemical in nature (Tran et al., 2017).

Thermodynamics describes the temperature dependence of the process. The thermodynamic parameters here, including enthalpy ΔH, entropy ΔS and Gibbs free energy ΔG, are shown in Table 3.

Table 3

Thermodynamic parameters regarding P adsorption onto CCM

T (°C)	Van't Hoff equation	K_C	ΔG (kJ/mol)	ΔH (kJ/mol)	ΔS (J/mol K)
22	y = -10664x + 50.33	1510798	-34.78	88.66	418.44
32	R^2 = 0.99	4254161	-38.96		
42		15047548	-43.15		

Coexisting anions can negatively influence adsorption processes, hence, to evaluate the selectivity of CCM for P removal the following (potentially competitive) anions NO_3^-, Cl^-, CO_3^{2-} and SO_4^{2-} were studied. As shown in Fig. 2a, in systems with coexisting anions, variable effects on P removal were noted (the negative influence of carbonate was most significant, causing ~30% reduction in adsorption). In mixtures where all these anions were present, P removal efficiency decreased from ~90% to ~45%.

285 Fig. 2b further shows the results of the P desorption experiments. The total potential
286 'calculated desorption capacity' was the sum of P desorption from unloaded samples
287 ($q_{b,des}$) and the P adsorption capacity of the CCM (q_{ads}). These were 28.61, 28.00 and
288 22.35 mg P/g for 0.5 M HCl, 2% citric acid and water, respectively. The experimental
289 desorption capacities using the P loaded CCM were 26.74, 26.84 and 0.62 mg P/g,
290 respectively. As such, only the water extraction was ineffective at removing the bound P.

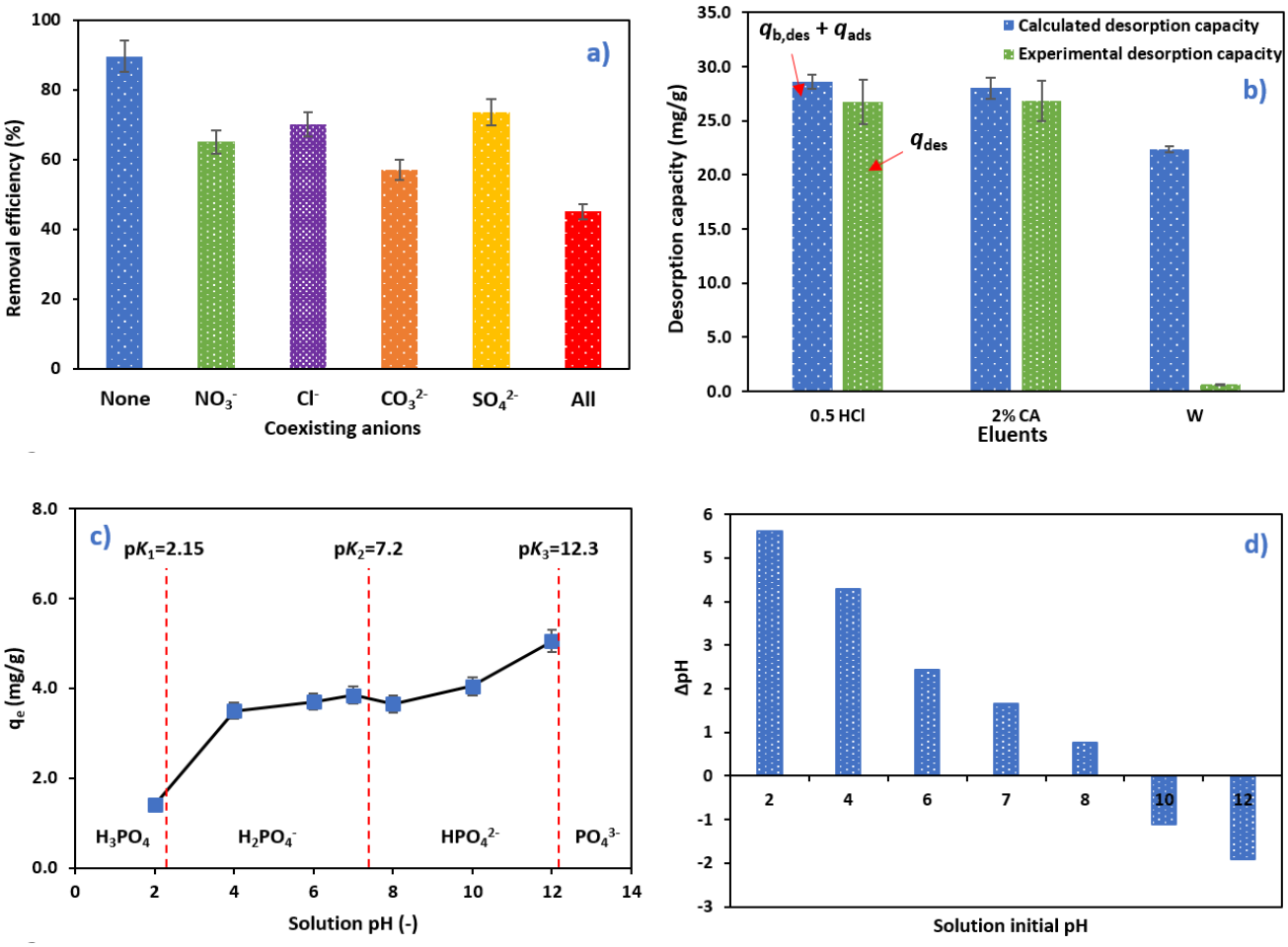

293 **Fig. 2.** Batch adsorption experimental results: (a) effect of coexisting ions, (b) P
294 desorption in water, 0.5 M HCl and 2% citric acid as eluents, (c) effect of pH and (d)
295 solution pH changes ($\Delta pH = pH_e - pH_{ini}$) during the adsorption onto CCM adsorbent
296 (initial concentration: 20 mg P/L; pH 2-12; contact time: 120 min; dose of adsorbent:

297 1 g/L; rotation speed: 150 rpm - Note: the data are represented as average ± standard
298 error).

299 The influence of solution pH on P adsorption by the CCM is shown in Fig. 2c. Adsorbed
300 P (mg P/g) increased rapidly with increased pH from 2.0 to 4.0, and then was relatively
301 stable between pH 4.0 - 10.0 then increasing again in the pH range 10.0 to 12.0. The pH
302 change ($\Delta pH = pH_{aft} - pH_{ini}$) during the P removal process is also shown on Fig. 2d. When
303 the initial pH of the solution was neutral (the municipal wastewater pH value was around
304 7), during the process the pH increased to pH ≈ 9, which indicates the alkali character of
305 the CCM ($pH_{pzc} = 8.78$).

306 *3.2. Characterisation of the CCM before and after P adsorption*

307 Fig. 3a-b gives the SEM micrographs with EDX analyses for the CCM before and after P
308 adsorption (CCM-P). The untreated CCM showed high EDX peaks (beyond carbon,
309 oxygen and nitrogen) for calcium, and potassium. After P adsorption, the potassium peak
310 disappeared, while a clear P peak appeared.

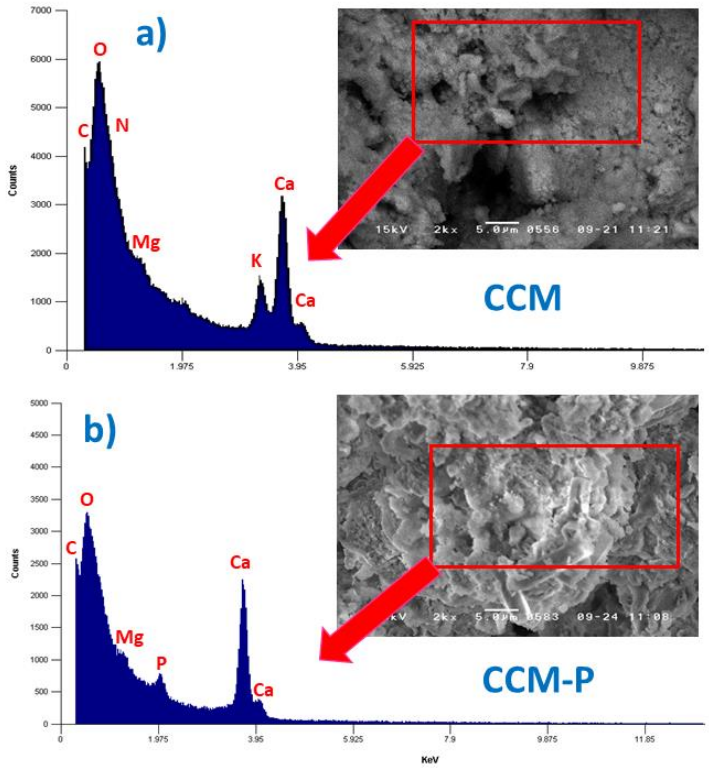

311

312 **Fig. 3.** SEM/EDX micrographs (a) before and (b) after adsorption (Note: CCM-P

313 represents the CCM adsorbent after P adsorption at P concentration of 50 mg P/L).

314 As shown in Fig. S3a, total pore volume and S_{BET} surface area of the P-loaded CCM

315 (0.084 cm^3/g and 12.97 m^2/g, respectively) was slightly less than for the untreated CCM

316 (0.086 cm^3/g and 13.629 m^2/g). The pore size distribution is also shown in Fig. S3b. It

317 can be seen that the CCM-P sample has a lower pore volume in the range between 50Å

318 (5nm) and 150Å (15nm) as compared to the unsaturated CCM adsorbent, suggesting

319 negligible pore filling during adsorption. The material can therefore be classified as a

320 mesoporous adsorbent (according to IUPAC). The point of zero charge (pH_{pzc}) of the

321 CCM was 8.78 (Fig. S3c). FTIR and XRPD results are presented on Fig. 4a and 4b

322 (discussed in section 4.2).

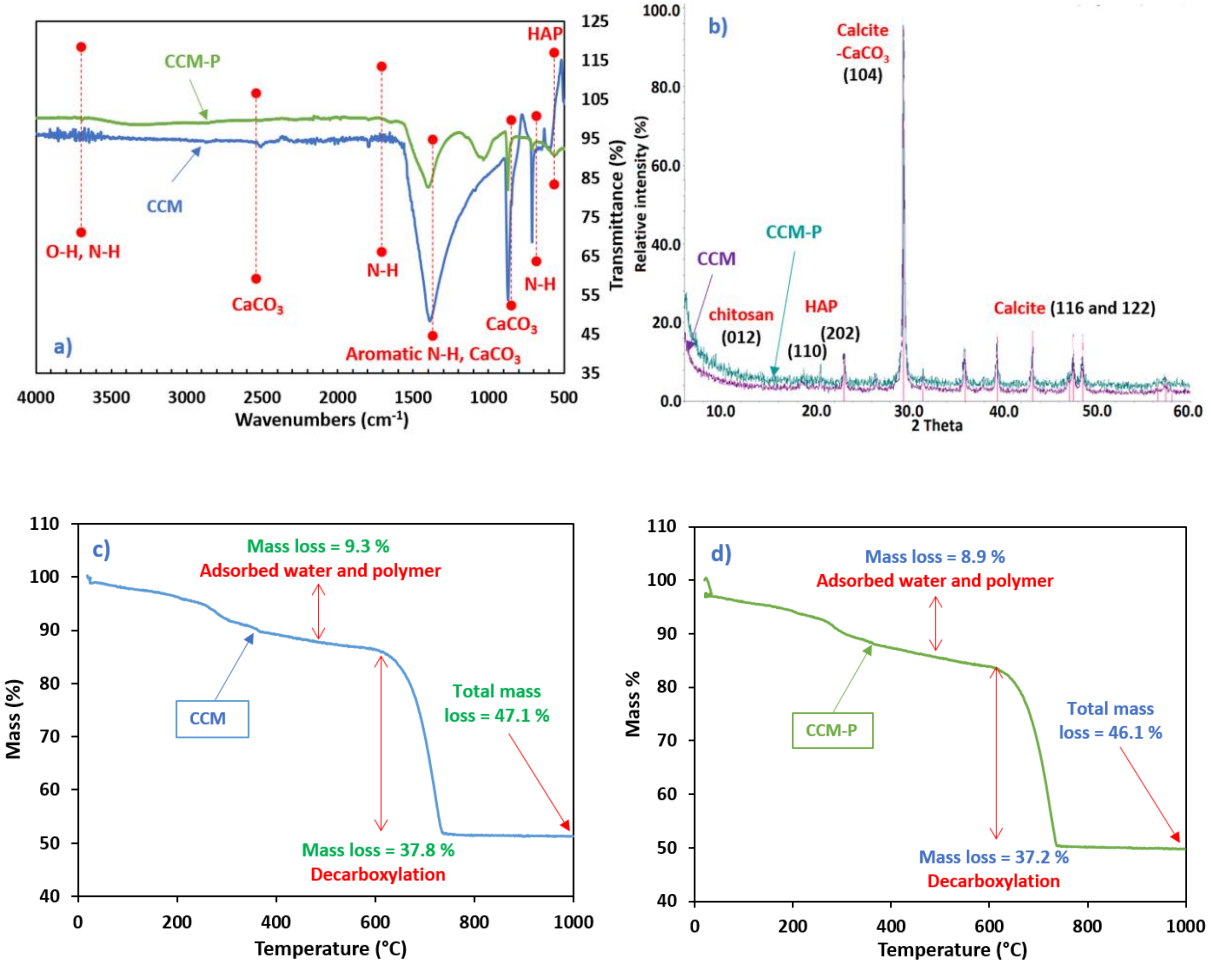

Fig. 4. Adsorbent characterisation results: (a) FTIR spectra, (b) XRPD pattern and (c-d) TGA curves of CCM and CCM-P (Note: the numbers in brackets on (b) are the Miller indices of the peaks; CCM-P represent the CCM adsorbent after P adsorption at P concentration of 50 mg P/L).

The thermogravimetric analysis (TGA) pre- and post-P adsorption (Fig. 4c-d) showed that the CCM had ≈9% weight loss over the range 216-378°C, and ≈37% loss in the range 601-741°C. Up to 378°C, weight loss was associated with moisture vaporisation (adsorbed water) and polymer degradation; rapid mass loss of 37% at 750°C, may be connected with decarboxylation of calcite.

3.3. Dynamic P adsorption onto CCM

Fig. 5a shows the adsorption performance of the CCM with various bed heights (3, 6, 10 cm), at a constant flow rate (7 mL/min) and inlet P concentration (10 mg P/L). Results for different operating conditions are shown in Table S2, which highlights improvements in performance with increasing bed height. Breakthrough time (t_b) increases from 0 to 305 min, while exhaustion time (t_e) increases from 530 to 845 min when the bed height increases from 3 to 10 cm. P adsorption capacity was also enhanced, with q_{eq} = 1.4 up to 2.2 mg P/g.

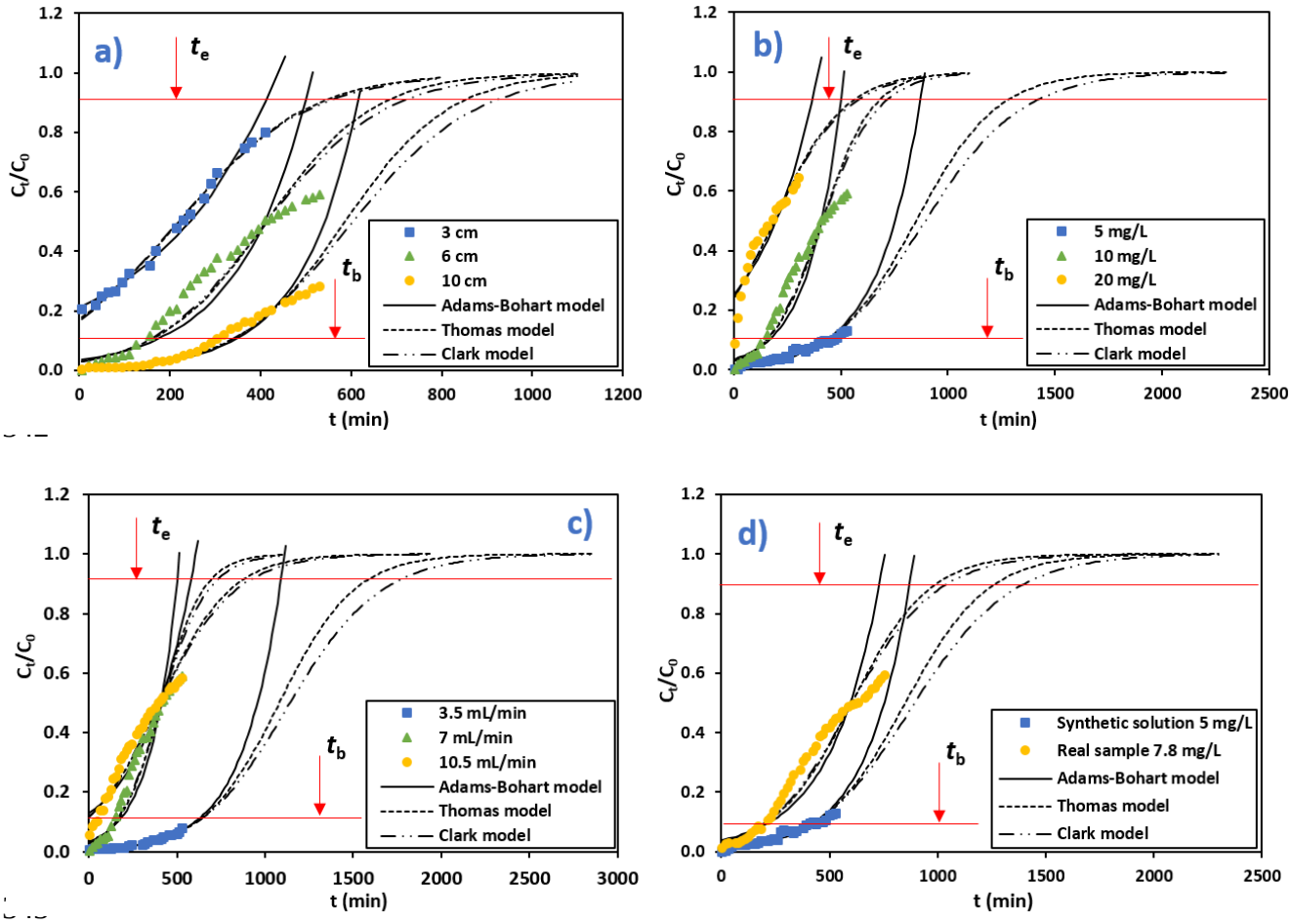

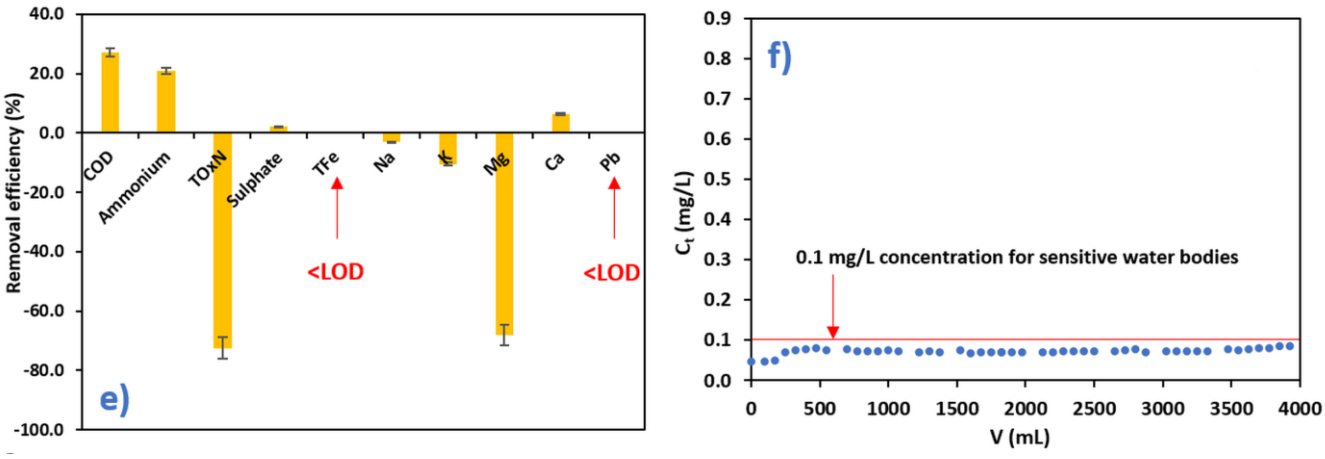

Fig. 5. Fixed-bed column adsorption experiments: effect of (a) bed height, (b) initial phosphate concentration and (c) flow rate (initial concentration: 5-20 mg P/L; no pH adjustment; flow rate: 3.5-10.5 mL/min; bed height: 3-10 cm); (d) spiked secondary wastewater effluent on breakthrough curves with three predicted dynamic models (breakthrough time (t_b) and exhaustion time (t_e)); (e) the metal/nutrient removal efficiency during adsorption with spiked secondary wastewater effluent (<LOD – below limit of detection) and (f) residual P concentrations after final (tertiary) wastewater effluent filtration (initial P concentration: 0.837 mg P/L).

The effect of initial P concentration (5, 10 and 20 mg P/L) on P removal performance was studied at a fixed CCM bed depth (6 cm) and flow rate (7 mL/min). As shown in Fig. 5b, the breakthrough curve becomes steeper as inlet P concentration increases. Further, the breakthrough time decreases (t_b = 485 to 0 min). Exhaustion time also declined with a rise in initial P concentration, from 1265 min (5 mg P/L) to 545 min (20 mg P/L) and, q_{eq} (equilibrium uptake) decreased from 2.4 to 1.9 mg P/g as the inlet P concentration increased.

360 The effect of flow rate (3.5, 7.0, and 10.5 mL/min) on P adsorption was investigated with
361 a constant bed height (6 cm) and initial P concentration of 10 mg/L. As Fig. 5c illustrates,
362 breakthrough time (t_b = 620 to 50 min) and exhaustion time (t_e = 1550 to 845 min) reduced
363 with increasing flow rate. The maximum capacity of the column decreased with increased
364 flow rate (q_{eq} = 2.3 to 2.0 mg P/g), as shown in Table S2.

365 Fig. 5d shows a comparison between spiked secondary WWTP effluent and a synthetic
366 solution, and the resultant breakthrough curves for similar conditions (flow rate of 7
367 mL/min; bed depth of 6 cm). The initial concentration of P was 7.8 mg P/L in the spiked
368 WWTP effluent and 5 mg P/L in the synthetic solution. During effluent filtration the
369 breakthrough and exhaustion time decreased from t_b = 485 to 245 min and t_e = 1265 to
370 1055 min, respectively. As expected, the adsorption capacity also decreased in the
371 presence of wastewater effluent (Table S2). CCM column tests indicated that the real
372 effluent had a 49 % shorter breakthrough time. Alongside the higher initial P
373 concentration in the wastewater, matrix effects clearly had an impact

374 To determine the potential for interference/competition, inorganic components (Fe, Pb,
375 Na, K, Mg, Ca, TOxN (Total Oxidised Nitrogen), sulphate, and ammonium and organic
376 matter (expressed as chemical oxygen demand, COD) were also measured before and
377 after effluent adsorption tests (Fig 5e). This revealed that TOxN, Mg, K and Na were
378 released from the CCM (due to the materials composition; Rae et al., 2019), while besides
379 P, 21.8% of the ammonium and 27.1% of the COD were removed.

380 To prove the utility of the CCM adsorbent, an additional trial was performed using
381 optimal conditions (flow rate of 7 mL/min and bed depth of 6 cm) with a low P final
382 (tertiary) WWTP effluent (at 0.837 mg P/L). As Fig. 5f illustrates, the CCM adsorbent

383 was capable of removing P even at these low concentrations, bringing the residual P level
384 below 100 µg/L. This in turn shows its applicability in terms of polishing low-P effluents
385 (i.e., its potential for use in preventing eutrophication in sensitive receiving waters).

386 Three widely used models (Adams-Bohart, Thomas, and Clark models) were used to
387 predict the dynamic behaviour of the column. The model parameters (determined from
388 the slopes and intercepts of the plots) are presented in Table S3. As seen in Table S3, the
389 R^2 values were higher (ranging from 0.84 to 0.99) and the corresponding χ^2 and RMSE
390 values lower for the Clark model, when compared to the other two models (indicating that
391 this model best predicts the breakthrough curve of the adsorption process).

392 **4. Discussion**

393 *4.1. Batch adsorption*

394 Giles et al. (1960) proposed a classification for adsorption isotherms depending on their
395 shape. In the work presented here, CCM isotherms for P adsorption were classified as L-
396 type (Langmuir) at lower temperatures and H-type (high affinity) at higher temperatures
397 (42°C). Both types are characterised by an initial concave region (relative to the
398 concentration axis; Tran et al., 2018), and by a high affinity towards P at low
399 concentrations (highlighting potential applicability in 'real-world' conditions). The good
400 Langmuir isotherm fit, implies that the adsorption of P onto CCM relates to monolayer
401 adsorption. This may be because modification of the CCM (with KOH) increased surface
402 homogeneity, creating a finite number of binding sites for P adsorption (Mitrogiannis et
403 al., 2017).

As shown in Fig. 1a, adsorption capacity was affected by solution temperature. The maximum monolayer adsorption capacity (q_{max}) calculated here was in the following order: 21.36 < 23.88 < 24.85 mg P/g at 22 < 32 < 42°C, respectively. This suggests that an energy increase in the adsorption system facilitated P adsorption (Tap Van et al., 2018). The increasing trend in P removal with increased temperature also highlights the endothermic nature of the process and potentially indicates applicability in warmer climates.

Further, CCM P adsorption capacity in this study was superior to that found in many other studies using similar materials (see Table 4).

Table 4

Comparison of adsorption capacity (q_{max}) for P using other adsorbents and synthetic solutions

Adsorbent material	q_{max} (mg P/g)	Reference
Oyster shell powder	0.21	(Chen et al., 2012)
Zinc(II)–chitosan biosorbent	6.55	(Yazdani et al., 2017)
Lime-iron sludge–encapsulated calcium alginate beads	8.30	(Chittoo and Sutherland, 2019)
Crawfish waste pyrolysed on low temperature	9.50	(Park et al., 2018)
Scallop shell synthesised ceramic biomaterial	13.60	(Chen et al., 2014)
Iron hydroxide-eggshell waste composite	14.49	(Mezenner and Bensmaili, 2009)
Finely-ground non-calcined mussel shell	18.23	(Paradelo et al., 2016)
Crosslinked Fe(III)-chitosan composites	15.84	(Zhang et al., 2018)
Calcined egg shell on 600 °C	19.23	(Panagiotou et al., 2018)
Crab carapace based chitosan-calcite adsorbent	**24.85**	**This study**
Chitosan-copper complex	35.50	(An et al., 2019)
Zirconium modified chitosan beads	60.60	(Liu and Zhang, 2015)

As shown in Fig. 1b, rapid adsorption of P to CCM was observed in the first 5 minutes, which suggested that P removal was initially controlled by outer-sphere surface complexation (electrostatic attraction). Numerous vacant adsorption sites (i.e., protonated OH and NH_2), and rapid diffusion (driven by the concentration gradient between the liquid/solid interface) will cause this rapid adsorption (Wang et al., 2016). Subsequently, adsorption slowed as other mechanisms, e.g., inner-sphere complexation (ligand exchange) and micro-precipitation began to be more dominant processes.

The PSO model (R^2 = 0.999) provided a better description of the experimental data than the PFO model (R^2 = 0.866–0.894), with evident differences in error function values (Table 2). The PSO model indicates that the adsorption of P onto CCM was chemisorption-dominated, involving valence forces via sharing or exchanging of electrons (as explained by Ho and McKay, 1998a; Ho and McKay, 1998b). Recently, studies have shown that adsorption behaviour which fits the PSO model well can often be explained by diffusion-based mechanisms as well (Hubbe et al., 2019). Similar results were reported for P adsorption onto crawfish char (Park et al., 2018) and an iron hydroxide-eggshell waste composite (Mezenner and Bensmaili, 2009).

In processes where intraparticle diffusion plays the only/major role in mass transfer, the plot of q_t versus $t^{1/2}$ (Fig 1c) will be a straight line with an intersection through the origin. However, as shown in Fig. 1c, mass transfer here exhibited three successive 'step-wise' straight lines (at both temperatures), none of which passed through the origin (thus, intraparticle diffusion was not the only mass transport limiting step here). The first rapid part of the process (film diffusion) describes the influence of strong electrostatic attraction on mass transfer; at the second stage (5-60 min), pore filling takes place at the inner surface of the CCM (intraparticle diffusion; wherein ligand exchange has the major

impact on mass transfer); then in the final phase (>60 min) equilibrium occurs (diffusion occurs slowly given the reduced concentration of P). Table 2 gives the parameters for the intraparticle diffusion model, where it can be observed that (for both temperatures) the value of k_i decreased with time. This proves that mass transfer was increasingly determined by intraparticle diffusion as time increased. Further, the value of C_i also increased with time indicating that the boundary layer effect also increased (Q. Yang et al., 2018). Finally, the rate constant parameters k_{i1}, and k_{i2} increased, while k_{i3} remained the same (with higher temperatures) suggesting an increase in mass-transfer to free adsorption sites and a decrease in intraparticle diffusion resistance (Jung et al., 2017).

From the thermodynamic data, calculated $+\Delta H$ and $+E_a$ values additionally highlight the endothermic nature of the adsorption process (resulting in increased adsorption capacity (Figs. 1a) and equilibrium constant (Table 1) at higher temperatures). In effect, ΔH for physisorption ranges from ~2.0 to 20 kJ/mol (Tran et al., 2016). As CCM with P exhibited a much higher ΔH value (88.66 kJ/mol), this suggests this process involves chemisorption. Further, ΔG values confirmed that adsorption occurred favourably and spontaneously and the low activation energy requirement (26.19 kJ/mol; from the kinetic study) further confirms these assertions. Finally, when the temperature increased from 22 to 42°C, ΔG and K_C values also dramatically increased indicating more energetically favourable adsorption at higher temperatures. The positive value of ΔS also confirms increased randomness and some structural changes at the solid/solution interface during the adsorption process (via surface microprecipitation).

4.2. Adsorption mechanisms

Since ‘real-world’ wastewater will always contain other anions, which can compete with P for adsorption sites and increase electrostatic repulsion between the adsorbent and P, it is important to consider such competition. From the anions tested here, NO_3^-, Cl^- and SO_4^{2-} caused decreases in P adsorption, most likely because these are non-specifically adsorbed, forming outer-sphere surface complexes with active sites and directly competing with P (Loganathan et al., 2014). Additionally, NO_3^- and Cl^- effects were more important (than for SO_4^{2-}) because of their smaller atomic size and higher mobility. In contrast, CO_3^{2-} drove a decrease in removal efficiency of ~33%, which was likely due to specific adsorption of carbonates - forming inner-sphere complexes with Ca^{2+} and hindering the formation of calcium phosphate precipitates on the CCM surface. Mitrogiannis et al. (2017) came to similar conclusions when studying the adsorption of P onto $Ca(OH)_2$ treated natural clinoptilolite. It must be emphasised though, that in secondary (normally final) WWTP effluent it is highly unlikely that all these anions will be at high enough concentrations to cause such significant reductions in the P adsorption capacity.

From the P release experiments performed here, high desorption when using 0.5M HCl eluent may indicate that inner-sphere complexation and surface precipitation were the major adsorption mechanisms involved. The adsorption process was seemingly slightly reversible in solutions with excess OH^- (i.e., distilled water at high pH 9.0, adjusted with NaOH), where OH^- ions presumably displaced P anions. This result confirmed that the electrostatic interaction between the P anions and the surface protonated hydroxyl and amine groups was not a major mechanism (Mitrogiannis et al., 2018; Tran et al., 2017). Common extraction tests used to assess plant availability of P utilise extraction in water, 2% citric acid and/or diluted mineral acids (Egle et al., 2016). Fig. 2b showed that almost

full desorption of P occurred with 2% citric acid, implying that the adsorbed P would be plant available if the CCM were to be used as a fertiliser for agricultural crops. Additionally, chitosan has been widely used in agriculture as a soil conditioner, it has antibacterial properties and the ability to chelate potentially deleterious metals (Zhang et al., 2018).

Results indicated that pH had a significant influence on P adsorption mechanisms and capacity. At low pH, low P adsorption was observed: likely because P was predominantly present as H_3PO_4 (rather than as negatively charged $H_2PO_4^-$). As pH increased within the range 2.15–7.2, anionic $H_2PO_4^-$ became the dominant species, increasing the efficiency of P adsorption onto positively charged sites via electrostatic interaction: the point of zero charge (pH_{pzc}) of the CCM was found to be 8.78 (Jung et al., 2017). With further increasing pH, OH^- ions may interfere directly with P adsorption; but this may be (partially) counteracted by favoured hydroxylapatite ($Ca_5(PO_4)_3(OH)$) precipitation on the CCM surface at pH 8-12 (a microprecipitation mechanism). Another important removal mechanism under these conditions was ligand exchange whereby $H_2PO_4^-$ and HPO_4^{2-} anions replaced CO_3^{2-} on the CCM surface and formed inner-sphere surface complexes (via Lewis acid-base interactions between P and ≡Ca-CO_3 groups; Mitrogiannis et al., 2017). P anions behave like Lewis bases, and can act as electron donors, donating electron pairs by binding to Ca atoms. At the same time, carbonate ions may be displaced into solution, driving pH increases (Fig. 2d) (Jiang et al., 2017). Fig. 2c shows that adsorption capacity in this system at pH 7 is only marginally less than in alkali conditions; as such, it would not be necessary to regulate water pH during a ‘real’ water treatment scenario - thus reducing the need for additional chemicals/reagents (and reducing operational costs).

509 Material characterisation was used to promote understanding of the mechanisms
510 governing adsorption. EDX data demonstrated the disappearance of the potassium (K)
511 peak in the P-loaded CCM sample (Fig 3a-b). One possible explanation for this is that the
512 K can interact additionally with P anions. This interaction can take place through reactions
513 between the monovalent anion $H_2PO_4^-$ (on the CCM surface) and K, forming potassium
514 dihydrogen phosphate as a soluble salt (Uzunova and Mikosch, 2016). In addition, Fig.
515 5e clearly indicated that (to some extent) dissolution of K into solution also occurred.

516 FTIR spectroscopy was used to characterise the functional groups on the raw CCM and
517 potentially highlight shifts caused by P bonding onto the CCM. The observed bands on
518 the FTIR spectra before and after P adsorption are shown in Fig. 4a. The broad stretching
519 vibration in the region of 3700–3500 cm^{-1} was attributed to the overlap between O-H and
520 N-H groups, which is observed in the FTIR spectrum of the sample after the adsorption
521 experiment. Additional N-H symmetric stretching peaked in the range 1800 cm^{-1} and 750
522 cm^{-1} was assigned to the amine groups. These nitrogenous and hydroxyl functional
523 groups on the chitosan almost disappeared after adsorption, suggesting that they were
524 involved in P adsorption through inner-sphere surface complexation. The strong
525 asymmetric band observed ~1400 cm^{-1} was assigned to C-N stretching vibration of
526 aromatic amines and the CO_3 of calcite (Arulvel et al., 2017). Aromatic amines have high
527 affinity for anions and are generally important in adsorbents. Due to P adsorption on these
528 protonated amine groups (on the chitosan chain), the intensity of this peak is reduced
529 significantly in P loaded CCM. Peaks ~900 cm^{-1} and ~2500 cm^{-1} confirmed the presence
530 of calcite ($CaCO_3$) in the CCM. Although it is difficult to get quantitative information
531 from band intensities, the obvious changes in the intensity of these peaks can be attributed
532 to a ligand exchange mechanism involving P anions and the CCM surface CO_3^{2-}. Weak

hydroxylapatite (HAP) stretches associated with P-O bonds that are found in HAP are seen in the range ~600 cm^{-1} on the saturated CCM. Because calcium is one of the main elements present on the CCM surface, this could react with P by crystallisation, forming Ca-P HAP crystals.

XRPD data is shown in Fig. 4b. The main crystalline phase identified in the CCM was calcite, with data matching well to the standard powder diffraction file 5-596 in the International Centre for Diffraction Data (ICDD) database (Swanson et al., 1953). This result was also consistent with the FTIR analysis (Fig. 4a). Broad diffraction peaks around 9.6° and 19° are likely due to the presence of the chitosan polymer. Visible differences between the diffraction patterns before and after adsorption were also observed, i.e., with respect to loss in crystallinity, causing peak broadening and reduced peak intensities (Rout et al., 2014; Shin et al., 2004). TGA analysis showed the P-loaded CCM to have similar thermal stability to that of the original material (Fig. 4c-d); while XRPD peaks at ~18.1° and 34.1° (for the P-loaded CCM after TGA) showed the presence of CaO and hydroxylapatite (Fig. S4).

Together, our results affirm that the crystallisation of P to form hydroxylapatite was a key mechanism contributing to P removal. Further, the desorption study and the PSO and Langmuir model data confirmed chemisorption of P onto the CCM, with microprecipitation of P occurring in the form of hydroxylapatite. Hydroxylapatite (as well as struvite), are existing slow release fertilisers (Talboys et al., 2016), which can act as substitutes for primary mined (and rapidly diminishing) rock phosphate reserves. The proposed adsorption mechanisms here are summarised in Fig. 6.

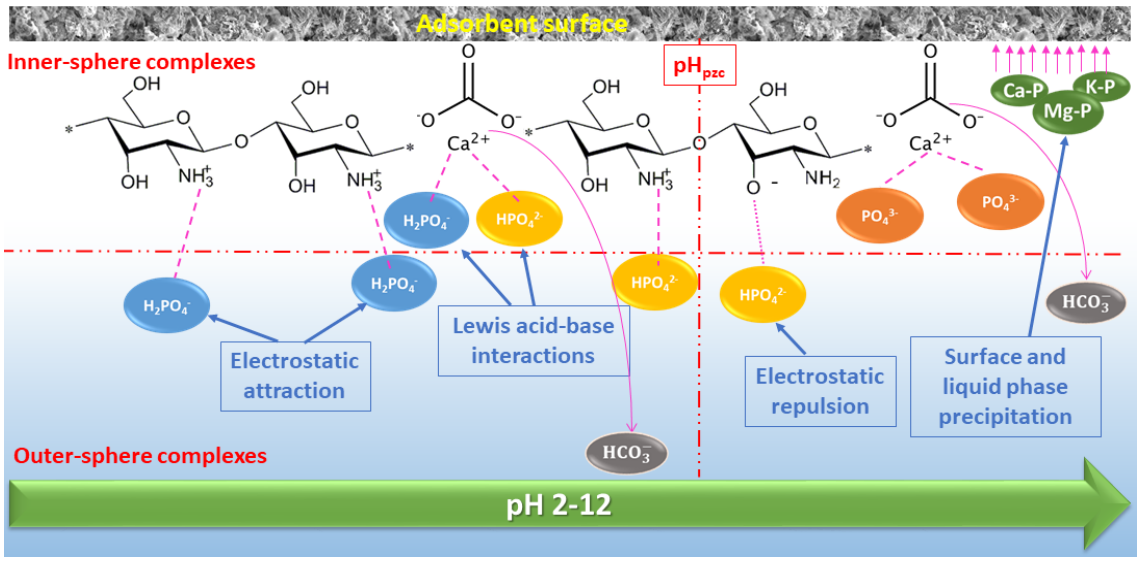

555

556 **Fig. 6.** Schematic of proposed adsorption mechanisms of P onto CCM adsorbent

557 *4.3. Dynamic study, scale-up design and cost analysis*

558 Greater bed height increased the total number of binding sites and solute residence time,
559 allowing P to more efficiently/effectively adsorb onto the CCM (Nguyen et al., 2015). A
560 greater bed height also allowed a longer contact time between the adsorbent and adsorbate
561 (1.3 – 4.5 min). Furthermore, the slope of the breakthrough curve (Fig. 5a) became flatter
562 with increasing bed height, resulting in a broadened mass transfer zone; i.e., the column
563 took longer to reach complete exhaustion (Sun et al., 2014).

564 Changes in flow-rate also significantly influenced the interaction between the CCM and
565 P, and the shape of the breakthrough curves. EBCTs were shortened with increased flow,
566 decreasing to 1.8 min at 10.5 mL/min. Hence, the process was incomplete, leading to
567 steep breakthrough data at the beginning of the adsorption process (Lim and Aris, 2014).
568 At a higher flowrate, as the external film mass-resistance at the surface of the adsorbent
569 tended to decrease, the residence time, and thus the saturation time, also decreased
570 resulting in a lower removal efficiency (Woumfo et al., 2015). Similarly, higher

adsorption capacity was attained at lower flow-rates, most probably due to increased residence time (for P) in the column. Since P had a longer contact time with the CCM, equilibrium could be reached before the P moved out of the column (Nguyen et al., 2015). Among the various breakthrough models tested in this study, the Clark model could be considered a more refined model as it involves both a mass-transfer concept in combination with the Freundlich isotherm. The Freundlich constant (*n* value) obtained was applied to estimate the Clark model parameters in this study. It is evident that the experimental breakthrough curves for P (at different column operating conditions) were well predicted by the Clark model over the entire period (Table S3). From the results, parameter *A* increased with bed depth, but decreased with initial P concentration and flow rate; whereas *r* values were low and close to each other, indicating a rapid and effective P mass transfer in the dynamically operated column. Increased bed-depth results in an increased number of particles for the P-CCM interaction, thereby, reducing the mass transfer rate (*r*). However, increased flow rate reduced molecular diffusion distance through the stationary layers of water surrounding the adsorbent particles thus intensifying the mass transfer rate (Sun et al., 2014). Similar trends in variation of the mass transfer rate have also been reported by other researchers (e.g. Rout et al., 2017).

While P adsorption using synthetic solutions has been the subject of many studies, there is still limited data regarding real wastewater samples (Zheng et al., 2019). Even secondary WWTP effluent can be challenging for adsorbent-based processes due to the presence of coexisting ions, dissolved organics and the potential impact of biofouling. Biofouling occurs when organic layers (made up of cells, molecules, detritus, and inorganic precipitates) form a barrier between the adsorbent surface and the water, reducing P uptake or the capacity of the adsorbent (Park et al., 2016). Here, biofouling

595 was not pronounced with this CCM (at least in the short term). Although breakthrough
596 time was shortened when using WWTP effluents, the CCM showed a selective affinity
597 towards P, based on specific adsorption mechanisms (as discussed). Additionally,
598 ammonium and COD were removed/reduced in the WWTP effluent, which suggests that
599 the CCM has potential to be used for this purpose. COD (indicative of organic matter)
600 may have an additional benefit, if this were to increase the organic carbon content of the
601 material, were it to be used as a fertiliser (assuming these organics are not undesirable
602 harmful contaminants).
603 Given the similarity in empty bed contact time (EBCT) and hydrodynamic characteristics
604 between a lab-scale experiment and either a pilot or full-scale system (Jung et al., 2017;
605 Yan et al., 2015), the effluent breakthrough data here can be further used to calculate the
606 parameters needed for a larger-scale column based process. The equations needed are
607 shown in Supplementary Material, and the scale-up design parameters are presented here
608 in Table 5.

609 **Table 5**

610 Parameters needed for large-scale column system

Parameters	Values
Filtration rate - *FR* (cm/min)	2.23
Diameter - *D* (cm)	35
Area –A_D (cm^2)	961.6
Bed height – H_{BD} (cm)	55
Bed volume – V_D (cm^3)	36,861
Flowrate – Q_D (L/h)	130
Adsorbent mass – M_D (kg)	15

As shown in Table 5, the key design parameters for a pilot-scale unit (diameter, area, and bed volume) were 35 cm, 961.6 cm^2, and 36,861 cm^3 respectively. In addition, a total volume of ≈500 L of wastewater could be treated before reaching the breakthrough time (t_b = 0.1, at around 245 min, with an initial concentration of 7.8 mg/L P) and ≈2,300 L to reach exhaustion time (t_e = 0.9, around 1055 min). Referring to Pap et al. (2020), the calculated cost involved in the production of this CCM is estimated at 0.561 US$/kg (561 US$/ton). According to current information, the cost of commercial adsorbents in the world market varies between ~800-5000 US$/ton (depending on the quality/type of adsorbent) (Selvaraju and Bakar, 2017). Using this production price, the adsorbent mass required, calculated adsorption capacity and treated effluent volume, the cost of treatment would be ~17 US$/$m^3$ or ~26 US$/kg P for a high P concentration effluent (i.e., 1-2 mg P/L; $q_{e,1\text{-}2mg/L}$ = 21.36 mg/g) and ~4 US$/$m^3$ or ~637 US$/kg P for a low concentration effluent (<0.1 mg P/L; $q_{e,<0.1\ mg/L}$ = 0.88 mg/g; see Supplementary Materials for calculations used) (Kumar et al., 2019). This is lower in comparison to 'classic' activated carbon filtration (50-200 US$/$m^3$) of treated wastewater, or 100–450 US$/$m^3$ for reverse osmosis, ion exchange or electrolysis (Gupta et al., 2012) and other P filtration processes (269 US$/kg P; Bashar et al., 2018). It should be noted that these data are preliminary and further optimisation would be needed before an industrial scale application could be undertaken. In addition, for all mentioned techniques the price shown includes only the operational costs (including chemicals), and not the total cost (i.e., including capital costs).

In future, we will test a Veolia™ Water Technologies UK designed FiltraPHOS™ Pilot Unit (Fig. S5) (using the conditions from Table 5) on an experimental wastewater treatment facility (Bo'Ness Development Centre, Scotland). The saturated-P rich material

obtained with real WWTP filtration will then be extensively tested for additional contaminants (i.e., full quality characterisation) together with real field/pot plant growth trials to observe phosphorous uptake/availability (alongside any potential contaminant uptake/availability). FiltraPHOS™ employs enhanced gravitational filtration through an adsorbent media with continuous self-backwashing. The proposed CCM adsorbent will be used as the filter media.

5. Conclusion

This study explored the feasibility of applying a crab carapace based adsorbent (a waste product from the fishing and food processing industry) to the removal and potential recovery of P. A low-cost low-temperature synthesis process was used to make a material with a high affinity towards phosphate, with structural strength, alkaline properties and rich in K. Different material characterisation methods were used on both fresh and P-laden adsorbent (CCM) material. Studies confirmed P to be effectively adsorbed onto the CCM under slightly alkaline conditions (pH>7) through mixed mechanisms, which included inner- and outer-sphere complexation and microprecipitation (as hydroxyapatite). The P-laden CCM is also amenable to efficient desorption (using 0.5 M HCl or 2% citric acid), indicating its potential to serve as slow-release P fertiliser/soil amendment material. Furthermore, when packed into fixed-bed columns, the CCM effectively removed P from secondary and final wastewater treatment plant effluent, under optimised conditions. Whilst further testing, upscaling and process optimisation is needed, the excellent performance of the CCM adsorbent (versus other materials previously studied for P removal) suggests the material merits further development. Its efficacy when applied to low P concentration final WWTP effluent was also

demonstrated, and scale-up cost estimates indicate that this material could provide a viable low-cost wastewater treatment option for P removal and recovery.

Declaration of competing interest

The authors declare that they have no known competing financial interests or personal relationships that could have appeared to influence the work reported in this paper.

Acknowledgments

This work was undertaken as part of the '*Phos4You*' project (NWE 292) with financial support from the INTERREG V B Northwest Europe programme. Authors are also thankful to Rebecca Rae for supporting FTIR and TGA analysis, Denny Morrison (Scottish Water) for provision of the wastewater effluent and Cedric Mebarki and Veolia™ Water Technologies UK for their help in pilot plant design, supply and construction.

Appendix A. Supplementary Materials

E-supplementary data for this work can be found alongside the online version of this paper.

References

Ajmal, Z., Muhmood, A., Usman, M., Kizito, S., Lu, J., Dong, R., Wu, S., 2018. Phosphate removal from aqueous solution using iron oxides: Adsorption, desorption and regeneration characteristics. J. Colloid Interface Sci. 528, 145–155. https://doi.org/10.1016/j.jcis.2018.05.084

Alshameri, A., Yan, C., Lei, X., 2014. Enhancement of phosphate removal from water by

679 TiO2/Yemeni natural zeolite: Preparation, characterization and thermodynamic.
680 Microporous Mesoporous Mater. 196, 145–157.
681 https://doi.org/10.1016/j.micromeso.2014.05.008
682 An, B., Lee, S., Kim, H.G., Zhao, D., Park, J.A., Choi, J.W., 2019. Organic/inorganic
683 hybrid adsorbent for efficient phosphate removal from a reservoir affected by algae
684 bloom. J. Ind. Eng. Chem. 69, 211–216. https://doi.org/10.1016/j.jiec.2018.09.029
685 APHA, 2005. Standard methods for the examination of water and wastewater, APHA,
686 AWWA, and WPCE. Am. Public Heal. Assoc. Springfield, New York Byrd Prog.
687 Arulvel, S., Elayaperumal, A., Jagatheeshwaran, M.S., 2017. Electroless nickel –
688 phosphorus coating on crab shell particles and its characterization. J. Solid State
689 Chem. 248, 87–95. https://doi.org/10.1016/j.jssc.2017.02.001
690 Bashar, R., Gungor, K., Karthikeyan, K.G., Barak, P., 2018. Cost effectiveness of
691 phosphorus removal processes in municipal wastewater treatment. Chemosphere
692 197, 280–290. https://doi.org/10.1016/j.chemosphere.2017.12.169
693 Bui, T.H., Hong, S.P., Yoon, J., 2018. Development of nanoscale zirconium molybdate
694 embedded anion exchange resin for selective removal of phosphate. Water Res. 134,
695 22–31. https://doi.org/10.1016/j.watres.2018.01.061
696 Chen, N., Hu, W., Feng, C., Zhang, Z., 2014. Removal of phosphorus from water using
697 scallop shell synthesized ceramic biomaterials. Environ. Earth Sci. 71, 2133–2142.
698 https://doi.org/10.1007/s12665-013-2618-2
699 Chen, W.T., Lin, C.W., Shih, P.K., Chang, W.L., 2012. Adsorption of phosphate into
700 waste oyster shell: Thermodynamic parameters and reaction kinetics. Desalin. Water
701 Treat. 47, 86–95. https://doi.org/10.1080/19443994.2012.696800
702 Chittoo, B.S., Sutherland, C., 2019. Adsorption Using Lime-Iron Sludge–Encapsulated

703 Calcium Alginate Beads for Phosphate Recovery with ANN- and RSM-Optimized
704 Encapsulation. J. Environ. Eng. 145, 04019019.
705 https://doi.org/10.1061/(asce)ee.1943-7870.0001519
706 Dai, L., Tan, F., Li, H., Zhu, N., He, M., Zhu, Q., Hu, G., Wang, L., Zhao, J., 2017.
707 Calcium-rich biochar from the pyrolysis of crab shell for phosphorus removal. J.
708 Environ. Manage. 198, 70–74. https://doi.org/10.1016/j.jenvman.2017.04.057
709 Du, L., Chen, Q., Liu, P., Zhang, X., Wang, H., Zhou, Q., Xu, D., Wu, Z., 2017.
710 Phosphorus removal performance and biological dephosphorization process in
711 treating reclaimed water by Integrated Vertical-flow Constructed Wetlands
712 (IVCWs). Bioresour. Technol. 243, 204–211.
713 https://doi.org/10.1016/j.biortech.2017.06.092
714 Egle, L., Rechberger, H., Krampe, J., Zessner, M., 2016. Phosphorus recovery from
715 municipal wastewater: An integrated comparative technological, environmental and
716 economic assessment of P recovery technologies. Sci. Total Environ. 571, 522–542.
717 https://doi.org/10.1016/j.scitotenv.2016.07.019
718 Furuya, K., Hafuka, A., Kuroiwa, M., Satoh, H., Watanabe, Y., Yamamura, H., 2017.
719 Development of novel polysulfone membranes with embedded zirconium sulfate-
720 surfactant micelle mesostructure for phosphate recovery from water through
721 membrane filtration. Water Res. 124, 521–526.
722 https://doi.org/10.1016/j.watres.2017.08.005
723 Giles, C.H., MacEwan, T.H., Nakhwa, S.N., Smith, D., 1960. 786. Studies in adsorption.
724 Part XI. A system of classification of solution adsorption isotherms, and its use in
725 diagnosis of adsorption mechanisms and in measurement of specific surface areas of
726 solids. J. Chem. Soc. 3973–3993.

Gupta, V.K., Ali, I., Saleh, T.A., Nayak, A., Agarwal, S., 2012. Chemical treatment technologies for waste-water recycling—an overview. Rsc Adv. 2, 6380–6388.

Haddad, K., Jellali, S., Jeguirim, M., Ben Hassen Trabelsi, A., Limousy, L., 2018. Investigations on phosphorus recovery from aqueous solutions by biochars derived from magnesium-pretreated cypress sawdust. J. Environ. Manage. 216, 305–314. https://doi.org/10.1016/j.jenvman.2017.06.020

Ho, Y S, McKay, G., 1998. A comparison of chemisorption kinetic models applied to pollutant removal on various sorbents. Process Saf. Environ. Prot. 76, 332–340. https://doi.org/10.1205/095758298529696

Ho, Y. S., McKay, G., 1998. Sorption of dye from aqueous solution by peat. Chem. Eng. J. 70, 115–124. https://doi.org/10.1016/S1385-8947(98)00076-X

Huang, H., Zhang, D.D., Li, J., Guo, G., Tang, S., 2017. Phosphate recovery from swine wastewater using plant ash in chemical crystallization. J. Clean. Prod. 168, 338–345. https://doi.org/10.1016/j.jclepro.2017.09.042

Hubbe, M.A., Azizian, S., Douven, S., 2019. Implications of Apparent Pseudo-Second-Order Adsorption Kinetics onto Cellulosic Materials : A Review. Bioresources 14, 7582–7626.

Jiang, D., Amano, Y., Machida, M., 2017. Removal and recovery of phosphate from water by a magnetic Fe 3 O 4 @ASC adsorbent. J. Environ. Chem. Eng. 5, 4229–4238. https://doi.org/10.1016/j.jece.2017.08.007

Jiang, H., Chen, P., Luo, S., Tu, X., Cao, Q., Shu, M., 2013. Synthesis of novel nanocomposite Fe3O4/ZrO 2/chitosan and its application for removal of nitrate and phosphate. Appl. Surf. Sci. 284, 942–949. https://doi.org/10.1016/j.apsusc.2013.04.013

751 Jung, K.W., Jeong, T.U., Choi, J.W., Ahn, K.H., Lee, S.H., 2017. Adsorption of
752 phosphate from aqueous solution using electrochemically modified biochar calcium-
753 alginate beads: Batch and fixed-bed column performance. Bioresour. Technol. 244,
754 23–32. https://doi.org/10.1016/j.biortech.2017.07.133
755 Kumar, A.S.K., Jiang, S.J., 2016. Chitosan-functionalized graphene oxide: A novel
756 adsorbent an efficient adsorption of arsenic from aqueous solution. J. Environ.
757 Chem. Eng. 4, 1698–1713. https://doi.org/10.1016/j.jece.2016.02.035
758 Kumar, P.S., Korving, L., van Loosdrecht, M.C.M., Witkamp, G.J., 2019. Adsorption as
759 a technology to achieve ultra-low concentrations of phosphate: Research gaps and
760 economic analysis. Water Res. X 4, 100029.
761 https://doi.org/10.1016/j.wroa.2019.100029
762 Lim, A.P., Aris, A.Z., 2014. Continuous fixed-bed column study and adsorption
763 modeling: Removal of cadmium (II) and lead (II) ions in aqueous solution by dead
764 calcareous skeletons. Biochem. Eng. J. 87, 50–61.
765 https://doi.org/10.1016/j.bej.2014.03.019
766 Liu, X., Zhang, L., 2015. Removal of phosphate anions using the modified chitosan beads:
767 Adsorption kinetic, isotherm and mechanism studies. Powder Technol. 277, 112–
768 119. https://doi.org/10.1016/j.powtec.2015.02.055
769 Loganathan, P., Vigneswaran, S., Kandasamy, J., Bolan, N.S., 2014. Removal and
770 recovery of phosphate from water using sorption. Crit. Rev. Environ. Sci. Technol.
771 44, 847–907. https://doi.org/10.1080/10643389.2012.741311
772 Lu, S., Gibb, S.W., Cochrane, E., 2007. Effective removal of zinc ions from aqueous
773 solutions using crab carapace biosorbent. J. Hazard. Mater.
774 https://doi.org/10.1016/j.jhazmat.2007.03.070

775 Mezenner, N.Y., Bensmaili, A., 2009. Kinetics and thermodynamic study of phosphate
776 adsorption on iron hydroxide-eggshell waste. Chem. Eng. J. 147, 87–96.
777 https://doi.org/10.1016/j.cej.2008.06.024
778 Mitrogiannis, D., Psychoyou, M., Baziotis, I., Inglezakis, V.J., Koukouzas, N., Tsoukalas,
779 N., Palles, D., Kamitsos, E., Oikonomou, G., Markou, G., 2017. Removal of
780 phosphate from aqueous solutions by adsorption onto Ca(OH)2treated natural
781 clinoptilolite. Chem. Eng. J. 320, 510–522.
782 https://doi.org/10.1016/j.cej.2017.03.063
783 Mitrogiannis, D., Psychoyou, M., Koukouzas, N., Tsoukalas, N., Palles, D., Kamitsos, E.,
784 Pantazidis, A., Oikonomou, G., Baziotis, I., 2018. Phosphate recovery from real
785 fresh urine by Ca(OH)2treated natural zeolite. Chem. Eng. J. 347, 618–630.
786 https://doi.org/10.1016/j.cej.2018.04.102
787 Nguyen, T.A.H., Ngo, H.H., Guo, W.S., Pham, T.Q., Li, F.M., Nguyen, T. V., Bui, X.T.,
788 2015. Adsorption of phosphate from aqueous solutions and sewage using zirconium
789 loaded okara (ZLO): Fixed-bed column study. Sci. Total Environ. 523, 40–49.
790 https://doi.org/10.1016/j.scitotenv.2015.03.126
791 Panagiotou, E., Kafa, N., Koutsokeras, L., Kouis, P., Nikolaou, P., Constantinides, G.,
792 Vyrides, I., 2018. Turning calcined waste egg shells and wastewater to Brushite:
793 Phosphorus adsorption from aqua media and anaerobic sludge leach water. J. Clean.
794 Prod. 178, 419–428. https://doi.org/10.1016/j.jclepro.2018.01.014
795 Pap, S., Kirk, C., Bremner, B., Turk Sekulic, M., Gibb, S.W., Maletic, S., Taggart, M.A.,
796 2020. Synthesis optimisation and characterisation of chitosan-calcite adsorbent from
797 fishery-food waste for phosphorus removal. Environ. Sci. Pollut. Res.
798 https://doi.org/10.1007/s11356-019-07570-0

Paradelo, R., Conde-Cid, M., Cutillas-Barreiro, L., Arias-Estévez, M., Nóvoa-Muñoz, J.C., Álvarez-Rodríguez, E., Fernández-Sanjurjo, M.J., Núñez-Delgado, A., 2016. Phosphorus removal from wastewater using mussel shell: Investigation on retention mechanisms. Ecol. Eng. 97, 558–566. https://doi.org/10.1016/j.ecoleng.2016.10.066

Park, J., Gill, G.A., Strivens, J.E., Kuo, L.J., Jeters, R.T., Avila, A., Wood, J.R., Schlafer, N.J., Janke, C.J., Miller, E.A., Thomas, M., Addleman, R.S., Bonheyo, G.T., 2016. Effect of biofouling on the performance of amidoxime-based polymeric uranium adsorbents. Ind. Eng. Chem. Res. 55, 4328–4338. https://doi.org/10.1021/acs.iecr.5b03457

Park, J.H., Wang, J.J., Xiao, R., Zhou, B., Delaune, R.D., Seo, D.C., 2018. Effect of pyrolysis temperature on phosphate adsorption characteristics and mechanisms of crawfish char. J. Colloid Interface Sci. 525, 143–151. https://doi.org/10.1016/j.jcis.2018.04.078

Paunovic, O., Pap, S., Maletic, S., Taggart, M.A., Boskovic, N., Turk Sekulic, M., 2019. Ionisable emerging pharmaceutical adsorption onto microwave functionalised biochar derived from novel lignocellulosic waste biomass. J. Colloid Interface Sci. 547, 350–360. https://doi.org/10.1016/j.jcis.2019.04.011

Rae, I.B., Gibb, S.W., Lu, S., 2009. Biosorption of Hg from aqueous solutions by crab carapace. J. Hazard. Mater. https://doi.org/10.1016/j.jhazmat.2008.09.052

Rae, I.B., Pap, S., Svobodova, D., Gibb, S.W., 2019. Comparison of sustainable biosorbents and ion-exchange resins to remove Sr 2+ from simulant nuclear wastewater: Batch, dynamic and mechanism studies. Sci. Total Environ. 650, 2411–2422. https://doi.org/10.1016/j.scitotenv.2018.09.396

Richardson, C.J., King, R.S., Qian, S.S., Vaithiyanathan, P., Qualls, R.G., Stow, C.A.,

2007. Estimating ecological thresholds for phosphorus in the Everglades. Environ. Sci. Technol. 41, 8084–8091. https://doi.org/10.1021/es062624w

Rout, P.R., Bhunia, P., Dash, R.R., 2017. Evaluation of kinetic and statistical models for predicting breakthrough curves of phosphate removal using dolochar-packed columns. J. Water Process Eng. 17, 168–180. https://doi.org/10.1016/j.jwpe.2017.04.003

Rout, P.R., Bhunia, P., Dash, R.R., 2014. Modeling isotherms, kinetics and understanding the mechanism of phosphate adsorption onto a solid waste: Ground burnt patties. J. Environ. Chem. Eng. 2, 1331–1342. https://doi.org/10.1016/j.jece.2014.04.017

Schröder, J.J., Smit, A.L., Cordell, D., Rosemarin, A., 2011. Improved phosphorus use efficiency in agriculture: A key requirement for its sustainable use. Chemosphere 84, 822–831. https://doi.org/10.1016/j.chemosphere.2011.01.065

Selvaraju, G., Bakar, N.K.A., 2017. Production of a new industrially viable green-activated carbon from Artocarpus integer fruit processing waste and evaluation of its chemical, morphological and adsorption properties. J. Clean. Prod. 141, 989–999. https://doi.org/10.1016/j.jclepro.2016.09.056

Shin, E.W., Han, J.S., Jang, M., Min, S.H., Park, J.K., Rowell, R.M., 2004. Phosphate Adsorption on Aluminum-Impregnated Mesoporous Silicates: Surface Structure and Behavior of Adsorbents. Environ. Sci. Technol. 38, 912–917. https://doi.org/10.1021/es030488e

Sun, X.F., Imai, T., Sekine, M., Higuchi, T., Yamamoto, K., Kanno, A., Nakazono, S., 2014. Adsorption of phosphate using calcined Mg3-Fe layered double hydroxides in a fixed-bed column study. J. Ind. Eng. Chem. 20, 3623–3630. https://doi.org/10.1016/j.jiec.2013.12.057

847 Swanson, H.E., Tatge, E., Fuyat, R., 1953. Standard X-ray Diffraction Powder Patterns.
848 Natl. Bur. Stand.
849 Talboys, P.J., Heppell, J., Roose, T., Healey, J.R., Jones, D.L., Withers, P.J.A., 2016.
850 Struvite: a slow-release fertiliser for sustainable phosphorus management? Plant Soil
851 401, 109–123. https://doi.org/10.1007/s11104-015-2747-3
852 Tap Van, H., Huong Nguyen, L., Dang Nguyen, V., Hoan Nguyen, X., Hai Nguyen, T.,
853 Vinh Nguyen, T., Vigneswaran, S., Rinklebe, J., Nguyen Tran, H., District, P., Chi
854 Minh City, H., 2018. Characteristics and mechanisms of cadmium adsorption onto
855 biogenic aragonite shells-derived biosorbent: Batch and column studies. J. Environ.
856 Manage. 1–0. https://doi.org/10.1016/j.jenvman.2018.09.079
857 Tran, H.N., Lin, C.C., Chao, H.P., 2018. Amino acids-intercalated Mg/Al layered double
858 hydroxides as dual-electronic adsorbent for effective removal of cationic and
859 oxyanionic metal ions. Sep. Purif. Technol. 192, 36–45.
860 https://doi.org/10.1016/j.seppur.2017.09.060
861 Tran, H.N., Wang, Y.F., You, S.J., Chao, H.P., 2017. Insights into the mechanism of
862 cationic dye adsorption on activated charcoal: The importance of Π–Π interactions.
863 Process Saf. Environ. Prot. 107, 168–180.
864 https://doi.org/10.1016/j.psep.2017.02.010
865 Tran, H.N., You, S.J., Chao, H.P., 2016. Thermodynamic parameters of cadmium
866 adsorption onto orange peel calculated from various methods: A comparison study.
867 J. Environ. Chem. Eng. 4, 2671–2682. https://doi.org/10.1016/j.jece.2016.05.009
868 Turk Sekulic, M., Boskovic, N., Milanovic, M., Letic, N.G., Gligoric, E., Pap, S., 2019.
869 An insight into the adsorption of three emerging pharmaceutical contaminants on
870 multifunctional carbonous adsorbent: Mechanisms, modelling and metal

871 coadsorption. J. Mol. Liq. 284, 372–382.
872 https://doi.org/10.1016/j.molliq.2019.04.020
873 Uzunova, E.L., Mikosch, H., 2016. Adsorption of phosphates and phosphoric acid in
874 zeolite clinoptilolite: Electronic structure study. Microporous Mesoporous Mater.
875 232, 119–125. https://doi.org/10.1016/j.micromeso.2016.06.019
876 Wang, S., Kong, L., Long, J., Su, M., Diao, Z., Chang, X., Chen, D., Song, G., Shih, K.,
877 2018. Adsorption of phosphorus by calcium-flour biochar: Isotherm, kinetic and
878 transformation studies. Chemosphere 195, 666–672.
879 https://doi.org/10.1016/j.chemosphere.2017.12.101
880 Wang, Z., Shen, D., Shen, F., Li, T., 2016. Phosphate adsorption on lanthanum loaded
881 biochar. Chemosphere 150, 1–7.
882 https://doi.org/10.1016/j.chemosphere.2016.02.004
883 Woumfo, E.D., Siéwé, J.M., Njopwouo, D., 2015. A fixed-bed column for phosphate
884 removal from aqueous solutions using an andosol-bagasse mixture. J. Environ.
885 Manage. 151, 450–460. https://doi.org/10.1016/j.jenvman.2014.11.029
886 Yan, L., Huang, Y., Cui, J., Jing, C., 2015. Simultaneous As(III) and Cd removal from
887 copper smelting wastewater using granular TiO2 columns. Water Res. 68, 572–579.
888 https://doi.org/10.1016/j.watres.2014.10.042
889 Yang, G., Wang, D., Yang, Q., Zhao, J., Liu, Y., Wang, Q., Zeng, G., Li, X., Li, H., 2018.
890 Effect of acetate to glycerol ratio on enhanced biological phosphorus removal.
891 Chemosphere 196, 78–86. https://doi.org/10.1016/j.chemosphere.2017.12.167
892 Yang, Q., Wang, X., Luo, W., Sun, J., Xu, Q., Chen, F., Zhao, J., Wang, S., Yao, F.,
893 Wang, D., Li, X., Zeng, G., 2018. Effectiveness and mechanisms of phosphate
894 adsorption on iron-modified biochars derived from waste activated sludge.

Bioresour. Technol. 247, 537–544. https://doi.org/10.1016/j.biortech.2017.09.136

Yazdani, M.R., Virolainen, E., Conley, K., Vahala, R., 2017. Chitosan-Zinc(II) complexes as a bio-sorbent for the adsorptive abatement of phosphate: Mechanism of complexation and assessment of adsorption performance. Polymers (Basel). 10, 1–19. https://doi.org/10.3390/polym10010025

Yeom, S.H., Jung, K.Y., 2009. Recycling wasted scallop shell as an adsorbent for the removal of phosphate. J. Ind. Eng. Chem. 15, 40–44. https://doi.org/10.1016/j.jiec.2008.08.014

Yu, Z., Zhang, C., Zheng, Z., Hu, L., Li, X., Yang, Z., Ma, C., Zeng, G., 2017. Enhancing phosphate adsorption capacity of SDS-based magnetite by surface modification of citric acid. Appl. Surf. Sci. 403, 413–425. https://doi.org/10.1016/j.apsusc.2017.01.163

Zhang, B., Chen, N., Feng, C., Zhang, Z., 2018. Adsorption for phosphate by crosslinked/non-crosslinked-chitosan-Fe(III) complex sorbents: Characteristic and mechanism. Chem. Eng. J. 353, 361–372. https://doi.org/10.1016/j.cej.2018.07.092

Zheng, Y., Wang, B., Wester, A.E., Chen, J., He, F., Chen, H., Gao, B., 2019. Reclaiming phosphorus from secondary treated municipal wastewater with engineered biochar. Chem. Eng. J. 362, 460–468. https://doi.org/10.1016/j.cej.2019.01.036